The Astrophysical Journal, 854:53 (15pp), 2018 February 10 https://doi.org/10.3847/1538-4357/aaa892

HD 104860 and HD 192758: Two Debris Disks Newly Imaged in Scattered Light with the *Hubble Space Telescope*

É. Choquet[1,2,10], G. Bryden[2], M. D. Perrin[3], R. Soummer[3], J.-C. Augereau[4], C. H. Chen[3], J. H. Debes[3], E. Gofas-Salas[5,6], J. B. Hagan[3], D. C. Hines[3], D. Mawet[1,2], F. Morales[2], L. Pueyo[3], A. Rajan[3], B. Ren[7], G. Schneider[8], C. C. Stark[3], and S. Wolff[9]

[1] Department of Astronomy, California Institute of Technology, 1200 E. California Boulevard, Pasadena, CA 91125, USA; echoquet@jpl.nasa.gov
[2] Jet Propulsion Laboratory, California Institute of Technology, 4800 Oak Grove Drive, Pasadena, CA 91109, USA
[3] Space Telescope Science Institute, 3700 San Martin Drive, Baltimore MD 21218, USA
[4] Université Grenoble Alpes, CNRS, IPAG, F-38000 Grenoble, France
[5] ONERA, The French Aerospace Lab, F-92322 Châtillon, France
[6] Institut de la Vision, F-75012 Paris, France
[7] Johns Hopkins University, 3400 North Charles Street, Baltimore, MD 21218, USA
[8] Steward Observatory, The University of Arizona, 933 North Cherry Avenue, Tucson, AZ 85721, USA
[9] Leiden Observatory, Leiden University, 2300 RA Leiden, The Netherlands
Received 2017 December 16; revised 2018 January 13; accepted 2018 January 15; published 2018 February 12

Abstract

We present the first scattered-light images of two debris disks around the F8 star HD 104860 and the F0V star HD 192758, respectively ∼45 and ∼67 pc away. We detected these systems in the F110W and F160W filters through our reanalysis of archival *Hubble Space Telescope* (*HST*) NICMOS data with modern starlight-subtraction techniques. Our image of HD 104860 confirms the morphology previously observed by *Herschel* in thermal emission with a well-defined ring at a radius of ∼114 au inclined by ∼58°. Although the outer edge profile is consistent with dynamical evolution models, the sharp inner edge suggests sculpting by unseen perturbers. Our images of HD 192758 reveal a disk at radius ∼95 au inclined by ∼59°, never resolved so far. These disks have low scattering albedos of 10% and 13%, respectively, inconsistent with water ice grain compositions. They are reminiscent of several other disks with similar inclination and scattering albedos: Fomalhaut, HD 92945, HD 202628, and HD 207129. They are also very distinct from brighter disks in the same inclination bin, which point to different compositions between these two populations. Varying scattering albedo values can be explained by different grain porosities, chemical compositions, or grain size distributions, which may indicate distinct formation mechanisms or dynamical processes at work in these systems. Finally, these faint disks with large infrared excesses may be representative of an underlying population of systems with low albedo values. Searches with more sensitive instruments on *HST* or on the *James Webb Space Telescope* and using state-of-the art starlight-subtraction methods may help discover more of such faint systems.

Key words: circumstellar matter – stars: individual (HD 104860, HD 192758) – techniques: image processing

1. Introduction

Debris disks are extrasolar system components evolving around main-sequence stars. They are composed of kilometer-sized planetesimals formed during the earlier protoplanetary stage of the system, and of dust particles generated by colliding bodies through a destructive grinding cascade stirred by secular perturbations from planets or large planetesimals (see Wyatt 2008 for a review). About 500 debris disk systems have been identified around nearby stars from their photometric excess in the infrared (Eiroa et al. 2013; Chen et al. 2014; Patel et al. 2017), revealing that massive dust systems are as common as 20% to 26% around A to K type stars in the solar neighborhood (Thureau et al. 2014; Montesinos et al. 2016).

Debris disks are the perfect laboratories to study the dynamical balance ruling circumstellar environments. Particles of different sizes, masses, and distances from their host stars are affected differently by the stellar radiation, wind, and gravity, and by perturbing bodies like substellar companions (Krivov 2010). Gravity is the dominant force for planetesimals and millimeter-sized grains, which orbit close to their parent bodies. Small particles, having a large cross-section compared to their volume, are on the other hand very sensitive to the radiative pressure and drag forces, and spread both inward and outward from their parent bodies on eccentric orbits. The smallest particles (submicron size) are blown out of the system by the stellar radiative pressure, resulting in an abrupt cutoff to the size distribution in debris disks and to their slow mass decay with time.

Resolved images of debris disks in several wavelength regimes provide ideal probes to study the dynamics in circumstellar environments. Images reveal the disks' morphology and the spatial distribution of their dust, and multi-wavelength imagery additionally traces particles of different sizes. As millimeter-sized grains are the most efficient emitters at long wavelengths, far-IR/millimeter images map the spatial distribution of the thermal emission of large grains and, indirectly, the location of their planetesimal parent bodies (e.g., Booth et al. 2016, 2017). Micron-sized particles are inefficient emitters, but efficiently scatter the starlight at wavelengths comparable to their size. Near-infrared and visible-light imaging thus shows how small dust grains spread out in debris disk systems (e.g., Schneider et al. 2014). By characterizing the spatial and size distributions of dust, multispectral imaging enables us to study the dynamical balance in disks as a function of the stellar environment (e.g., MacGregor et al. 2017).

[10] Hubble Fellow.

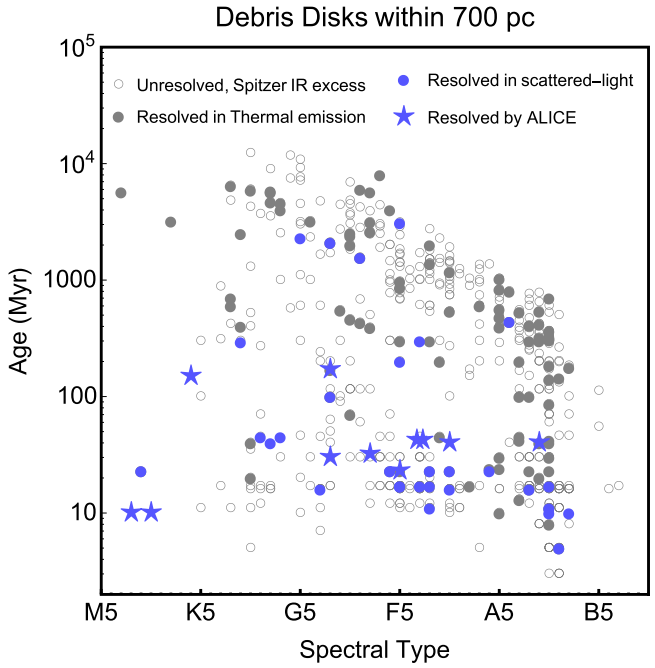

Figure 1. Age and spectral type distribution of the 500 stars within 700 pc with a debris disk detected in thermal emission by the *Spitzer Space Telescope* (gray empty circles; Chen et al. 2014) and/or that have been resolved in thermal emission (gray filled circles, 97 systems) or in scattered light (blue markers, 41 systems). The blue stars highlight the debris disks first imaged by ALICE in scattered light. We note that the *Spitzer* sample is 94% composed of stars within 250 pc, with only a few systems beyond 500 pc.

Furthermore, resolved images let us study possible planet–disk interactions by characterizing the imprints of unseen planets on the disk morphologies (Lee & Chiang 2016). Giant gaseous planets, although rare at 10–100 au, are more commonly found in systems harboring massive debris disks (Meshkat et al. 2017).

About a hundred debris disks have been spatially resolved to date, mostly in thermal emission at 70–160 μm with the *Herschel Space Observatory* (e.g., Booth et al. 2013; Eiroa et al. 2013; Matthews et al. 2014; Morales et al. 2016; Vican et al. 2016) or at submillimeter/millimeter wavelengths with JCMT (Holland et al. 2017) and ALMA (e.g., MacGregor et al. 2013, 2016a; Su et al. 2017). Using the measured radii of a sample of *Herschel*-resolved disks, Pawellek et al. (2014) interestingly showed that the typical grain size in these disks does not directly scale with the radiative pressure blowout particle size, but decreases with stellar luminosity. This may indicate that other mechanisms are at work in debris disks that limit the production of small grains around late stars or that induce a higher level of excitation and planetesimal stirring around early stars (Pawellek & Krivov 2015).

Such hypotheses could be tested by studying the small dust population in debris disks with scattered-light imaging. However, about 40 debris disks have been resolved so far in scattered light, and only half of these have also been resolved in thermal emission (see Figure 1). Resolving disks in this wavelength regime is technically challenging, as the star is typically 1000 times brighter than the total disk emission at these wavelengths, and the disks, typically within a few arcseconds of their host star, are buried within the bright and temporally varying diffraction pattern.

In this paper, we report the detection of two new debris disks in the scattered-light regime. They were identified through our reanalysis of archival coronagraphic data from the *Hubble Space Telescope* (*HST*) NICMOS instrument as part of the Archival Legacy Investigations of Circumstellar Environments (ALICE) project,[11] using modern starlight-subtraction techniques to reveal the faint disk emissions. The disk around HD 104860 has been previously resolved in thermal emission with *Herschel*-PACS at 100 and 160 μm (Morales et al. 2013, 2016), but that around HD 192758 has not been resolved so far. These two new detections bring the number of debris disks first imaged in scattered light by the ALICE program to 11, demonstrating the efficacy of our post-processing method in detecting faint resolved circumstellar material (Soummer et al. 2014; Choquet et al. 2016, 2017). Along with the five debris disks detected during its operational time, NICMOS currently holds the record of the most debris disks first imaged in scattered light.

In Section 2, we present the data sets used in this work and the data reduction process. Section 3 presents the two systems HD 104860 and HD 192758, and describes the debris disk detections. We present our analysis of the disk morphologies in Section 4.

2. Data Sets and Data Processing

2.1. Data Sets

The data on HD 104860 and HD 192758 were obtained as part of two surveys with the near-IR NICMOS instrument on *HST* that aimed to resolve a selection of debris disks identified from their infrared excess with the *Spitzer Space Telescope* (HST-GO-10527, PI: D. Hines) and with *IRAS*/*Hipparcos* (HST-GO-11157, PI: J. Rhee), respectively. The data were all obtained with the intermediate-sampling camera NIC2 ($0\farcs07565$ pixel^{-1}) and with its coronagraphic mode featuring a $0\farcs3$ radius occulting mask.

HD 104860 was observed in two telescope orientations, with the spacecraft rolled by 30° to enable the subtraction of the coronagraphic point-spread function (PSF) through roll differential imaging (Lowrance et al. 1999). HD 192758 was also observed in two 30° different rolls on 2007 July 03, then again in two other rolls about a year later (UT 2008 June 04). However, the guide star acquisition failed during one roll of the later observing sequence, and none of the integrations within this roll were acquired with the star centered on the occulting spot. We only used exposures from the three successful roll acquisitions in our study, and we combined data from both epochs to maximize the signal-to-noise ratio (S/N) on the detection, as we do not expect significant temporal variations in the disk morphology and photometry.

HD 104860 was observed with the NICMOS F110W filter, and HD 192758 with both the F110W and F160W filters. These two wideband filters were the most commonly used for NICMOS coronagraphic observations, which facilitated assembling large and homogeneous PSF libraries for advanced post-processing (Hagan et al. 2018). The F160W NICMOS filter (pivot wavelength 1.600 μm, 98% integrated bandwidth 0.410 μm) is comparable to the ground-based *H* bandpass, while the NICMOS F110W filter (pivot wavelength 1.116 μm, 98% integrated

[11] https://archive.stsci.edu/prepds/alice/

Table 1
Observing and Processing Parameters

Parameters	HD 104860 (F110W)	HD 192758 (F110W)	HD 192758 (F160W)
UT date	2006 Mar 20	2007 Jul 03 2008 Jun 04	
No. of orientations	2	3	
Orientation difference (°)	30	30; 2; 28	
Filter	F110W	F110W	F160W
λ_p (μm)	1.116	1.116	1.600
F_ν (μJy.s.DN^{-1})	1.21121	1.21121	1.49585
No. of combined frames	18	15	15
Total exp. time (s)	5183	3456	3456
No. of frames in PSF library	439	327	277
No. of subtracted PCs	141	130	80
Image crop size (pix)	140	80	80
Mask radius (pix)	13	8	8

bandwidth 0.584 μm) is twice as extended toward shorter wavelengths as the *J* band.

The observing parameters and instrument characteristics of the three data sets (HD 104860 (F110W), HD 192758 (F110W), and HD 192758 (F160W)) are summarized in Table 1.

2.2. Data Processing

To detect the signal of the disks, which is fainter compared to the star, we used the multi reference-star differential imaging (MRDI) PSF subtraction method developed for the ALICE program (Soummer et al. 2011; Choquet et al. 2014). We assembled and registered large and homogeneous libraries of coronagraphic images from the NICMOS archive, gathering images from multiple reference stars observed as part of several *HST* programs. These libraries were used to subtract the star PSF from each exposure of the science target with the Principal Component Analysis (PCA) KLIP algorithm (Soummer et al. 2012).

All of the images used to process the HD 104860 data set (PSF library and science images) were calibrated with contemporary flat-field images and observed dark frames as part of the Legacy Archive PSF Library and Circumstellar Environments (LAPLACE) program.[12] Conversely, HD 192758's data were obtained in *HST* cycle 16, the last operational cycle of NICMOS, and were not included in the LAPLACE calibration program. To have libraries large enough to sample the PSF variations as well as representative of HD 192758's images, we assembled PSF libraries both from LAPLACE programs and from the non-LAPLACE HST-GO-11157 program. The latter was processed with the NICMOS `calnica` calibration pipeline and bad pixel corrected. For HD 104860's and HD 192758's data sets, we respectively down-selected 60% and 30% of the images in the libraries most correlated with their respective science frames. This selective criterion ensures that the images in the libraries are well representative of the star PSF in each science frame (Choquet et al. 2014), and minimizes the oversubtraction of the astrophysical signal, especially in the case of extended objects, which project more strongly on poorly matched PSF components with PCA-type algorithms.

[12] https://archive.stsci.edu/prepds/laplace

We applied the KLIP algorithm to the cropped sub-images of the science target excluding a central circular area. The number of principal components (PCs) used for the PSF subtraction was selected to maximize the S/N on the disks after visual inspection of the final images. The PSF-subtracted exposures were then rotated to have north pointing up, co-added, and scaled to surface brightness units based on the exposure time, *HST*'s calibrated photometric factors (F_ν), and plate scale. The post-processing parameters (crop size, mask radius, PSF library size, number of PCs) are listed in Table 1.

To estimate the noise in the final images, we processed the reference star images from the PSF libraries with the same method and reduction parameters as the science images. The PSF-subtracted libraries were then partitioned into sets with the same number of frames as the science targets, rotated with the target image orientations, and combined. The noise maps were computed from the pixel-wise standard deviation across these sets of processed reference star images.

3. Disk Detections

We detect faint and resolved dust emission around both stars. Figure 2 presents the images of the two disks and their respective S/N maps. We list some properties of the two systems in Table 2.

3.1. HD 104860

HD 104860 is an F8 field star at 45.0 ± 0.5 pc (Gaia Collaboration et al. 2016). Its age was estimated, based on its chromospheric activity, to be 32 Myr by Hillenbrand et al. (2008), and to be 19–635 Myr by Brandt et al. (2014). The system has a significant infrared excess at 70 μm identified with *Spitzer* with a fractional infrared luminosity of $L_{\rm dust}/L_\star \sim 6.3 \times 10^{-4}$ (Hillenbrand et al. 2008). Its SED is well-described by a two-temperature blackbody model, with a warm dust population at 210 ± 27 K with a fractional luminosity of 2.4×10^{-5} and a cold dust population at 42 ± 5 K with a large infrared fractional luminosity of 2.8×10^{-4} (Chen et al. 2014). Without a prior on the dust separation to the star and assuming that the disks are in radiative and collisional equilibrium, these blackbody emissions correspond, respectively, to a $\sim 10^{-5}\,M_{\rm Moon}$ disk at a radius of 3 au from the star, and to a massive $\sim 1.5\,M_{\rm Moon}$ cold disk at a radius of 366 au, based on silicate spherical grain compositions. By measuring the cold disk spectral index in the millimeter from VLA and ATCA observations, MacGregor et al. (2016b) estimated a dust size distribution in the system with a power-law $q = 3.64 \pm 0.15$, consistent with steady-state collisional cascade models (Dohnanyi 1969; Gáspár et al. 2012; Pan & Schlichting 2012). Assuming a disk composed of astro-silicates (Draine 2003), a stellar luminosity of $L_\star = 1.16\,L_\odot$, and mass of $M_\star = 1.04\,M_\odot$, the radiative pressure blowout grain size limit is estimated as $a_{\rm blow} \sim 0.4$ μm, but the minimum grain size is inferred to be ~ 7 μm from joint modeling of the system's SED and *Herschel* images (Pawellek et al. 2014).

The disk was first resolved in thermal emission at 100 and 160 μm with *Herschel*-PACS (Morales et al. 2013) then marginally resolved at 1.3 mm with CARMA (Steele et al. 2016). The *Herschel* image at 100 μm shows a disk of radius 116 ± 6 au, three times smaller than the radius inferred from SED modeling, and inclined by $54° \pm 7°$ from face-on

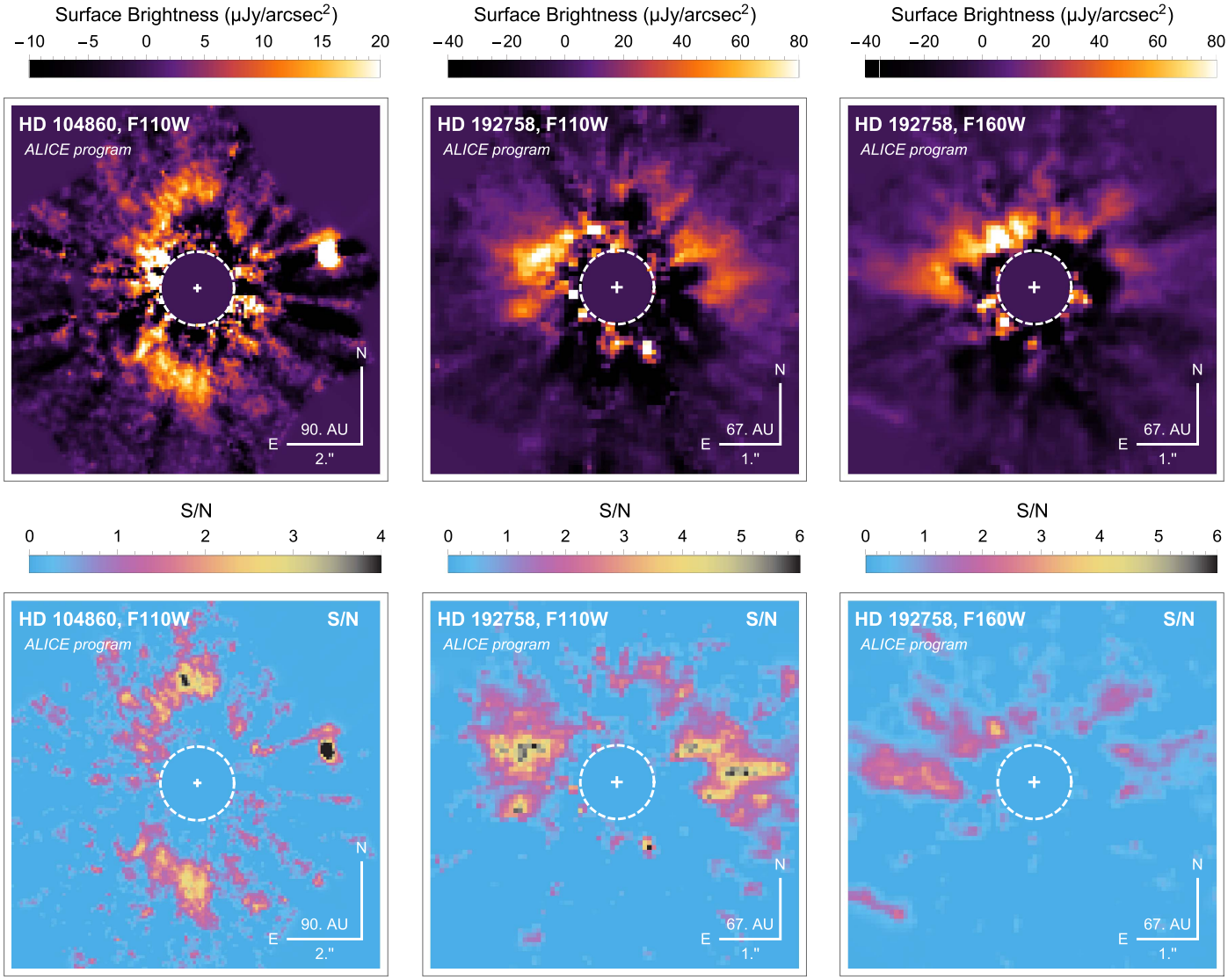

Figure 2. Debris disks detected around HD 104860 (F110W filter) and HD 192758 (F110W and F160W filters) by reanalyzing archival *HST*-NICMOS data as part of the ALICE program, using libraries built of multiple reference star images from the NICMOS archive and using the PCA-KLIP algorithm. The top row shows the disk images in surface brightness units, and the bottom row shows the S/N maps. All images have been smoothed by convolution with a synthetic PSF. The white dashed circles show the area masked for post-processing with KLIP.

Table 2
System Properties

Properties	HD 104860	HD 192758
R.A. (J2000)	12 04 33.731	20 18 15.790
Decl. (J2000)	+66 20 11.715	−42 51 36.297
Spectral Type	F8	F0V
J (mag)	6.822 (1)	6.387 (1)
H (mag)	6.580 (1)	6.298 (1)
Distance (pc)	45.0 ± 0.5 (2)	67 ± 2 (2)
PM R.A. ($''$/yr)	−57.07 ± 0.06 (2)	51.65 ± 0.07 (2)
PM Decl. ($''$/yr)	43.7 ± 0.3 (2)	−57.9 ± 0.4 (2)
Age (Myr)	19–635 (3, 4)	45–830 (5, 6)
Association	Field (4)	Field/ICS 2391 (5, 6)
$L_{dust}/L_{\star}$	6.3×10^{-4} (3)	5.7×10^{-4}(7)

References. (1) Cutri et al. (2003), (2) Gaia Collaboration et al. (2016), (3) Hillenbrand et al. (2008), (4) Brandt et al. (2014), (5) Moór et al. (2006), (6) Chen et al. (2014), (7) Moór et al. (2011).

with a position angle (PA) of 1° ± 7°. Such a significant difference in radius between observations and SED modeling is found for many resolved systems and stresses the need for resolved images to put constraints on debris disk properties. Using the radius inferred from the *Herschel* image to constrain SED modeling, Morales et al. (2016) found that both pure astro-silicate grains and a mixture of water ice and astro-silicates could compose the dust in the system.

In our F110W NICMOS image, we detect a large ring-shape debris disk around HD 104860 with a radius of ∼112 au (∼2.″5), inclined by ∼60° from face-on. The disk is detected at S/N ∼ 2–4 per pixel and S/N ∼15 integrated over the disk area detected above 1.5σ. This detection enables us to put strong constraints on the disk's general morphology (see Section 4), but the S/N is too low to reliably comment on the substructures within the disk. The observed morphology largely agrees with the *Herschel* thermal emission image, with a 60 times better

Table 3
Point Source Astrometry Around HD 104860

Epoch (UT date)	Separation (″)	P.A. (°)	References
2002 Jun 23	3.803 ± 0.027	−72.99 ± 0.28	1
2006 Mar 20	3.50 ± 0.08	−75.6 ± 1.2	2
2013 Jan 27	3.14 ± 0.01	−80.2 ± 0.2	2

References. (1) Metchev & Hillenbrand (2009), (2) this work.

angular resolution (95 mas versus 5.″9 resolution), and provides the first image of the dust in the scattered-light regime. The east side is significantly brighter than the west side, indicative of anisotropic scattering from the dust and showing the near side of the disk, assuming grains preferentially forward-scatter. Our image unambiguously reveals a cleared cavity from the disk's inner edge and down to ∼45 au from the star, which we further characterize in Section 4.

We detect a bright point source ∼3.″5 northwest from the star. We report its astrometry in Table 3. We identify it as candidate #1 detected in Metchev & Hillenbrand (2009), and we confirm that its astrometry is consistent with a background star, as noted by the authors. We note that this object is wrongly reported as a binary companion in the Washington Double Star catalog (WDS 12046 +6620AB). To further confirm the background nature of this point source, we reprocessed a Keck-NIRC2 archival data set acquired on UT 2013 January 27 using the K' filter (program N117N2, PI: F. Morales). After standard processing and registration steps, we detect the point source using the classical Angular Differential Imaging (Marois et al. 2006) PSF subtraction method. We report the measured astrometry of the point source relative to HD 104860 in Table 3. The point source indeed follows the background track between the three epochs, although we note a significant shift between the measured position and the background-track-predicted astrometry over the 11 year baseline that is likely due to the background star's own proper motion (see Figure 3).

3.2. HD 192758

HD 192758 is an F0V star at 67 ± 2 pc (Gaia Collaboration et al. 2016). Moór et al. (2006) reported a 50% probability for the star, of age 50 ± 5 Myr, to be a member of the IC 2391 supercluster (Navascués et al. 2004). On the other hand, Chen et al. (2014) found the system to be a field star of isochronal age ∼830 Myr. The system has a fractional infrared excess around 100 μm with $L_{\rm dust}/L_\star \sim 5.6 \times 10^{-4}$ (Moór et al. 2006). It is well modeled by a two-temperature blackbody emission, with a warm disk at 164 ± 7 K with a fractional luminosity of $\sim 0.38 \times 10^{-4}$ and a cold dust belt at 54 ± 6 K with a fractional luminosity of $\sim 4.1 \times 10^{-4}$ (Chen et al. 2014). Assuming the disks to be in radiative and collisional equilibrium and composed of silicate spherical spheres, these blackbody emission corresponds to dust belts of mass $\sim 1.3 \times 10^{-4}\, M_{\rm Moon}$ and $\sim 8.7 \times 10^{-1}\, M_{\rm Moon}$, respectively, and at radii ∼6 au and ∼152 au, respectively.

We spatially resolve the outer disk in HD 192758 in both the F110W and the F160W data sets. In the F110W image, the disk is detected up to S/N ∼ 6 per pixel, and S/N ∼ 45 integrated over the pixels above 1.5σ. In F160W, the detection is found with S/N up to ∼4 per pixel, and with S/N ∼ 21 integrated over the disk area above 1.5σ. The disk presents a similar morphology in the two images. They both reveal a disk of radius ∼100 au (∼1.″5) and inclined by ∼60°

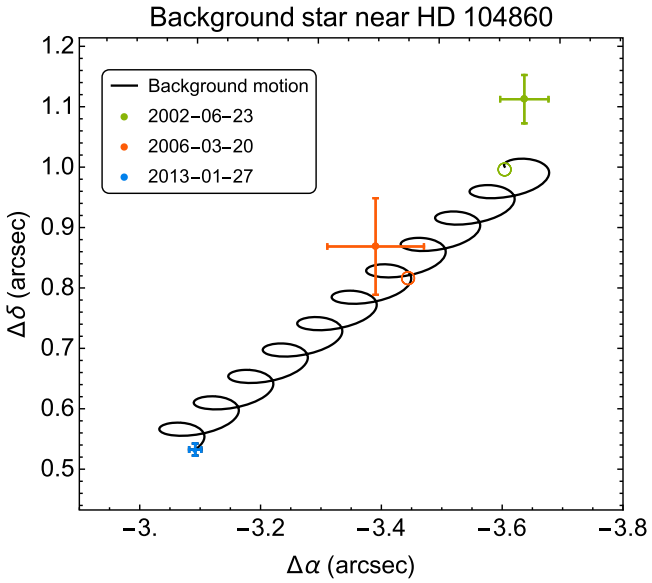

Figure 3. Astrometry of the point source relative to HD 104860, measured with Palomar-P1640 on 2002 June 23 (green) from Metchev & Hillenbrand (2009), *HST*-NICMOS on 2006 March 20 (orange), and Keck-NIRC2 on 2013 January 27 (blue). The black line shows the relative motion of a fixed background object from the point source position at epoch 2013 January 27. The unfilled circles indicate the predicted background position at the corresponding epoch. The point source measured astrometry follows the background track and is not co-moving with HD 104860.

from face-on. As for HD 104860, the disk radius is significantly smaller than the disk radius estimated from SED modeling, which stresses again the need for imaging to put reliable constraints on disk properties. The south side of the disk is not detected, which also indicates anisotropic scattering by the dust grains, presumably showing the near side of the disk north of the star.

4. Disk Modeling

PSF subtraction with algorithms that solve the least-squares problem of minimizing the residuals between the science image and a set of eigenimages systematically involves some level of oversubtraction of circumstellar materials, along with the PSF (Lafrenière et al. 2007; Soummer et al. 2012; Pueyo 2016). This effect biases both the morphology and the photometry of circumstellar sources, and the effect depends on the shape of the source and of the reduction parameters. For extended objects in ALICE-processed NICMOS data, the algorithm throughput typically ranges from 20% at 0.″5 from the star to 80% at large separations, in the case of a face-on ring-like disk.

Calibrating the effect of the algorithm throughput is critical to properly characterize the morphology of extended sources and to estimate their unbiased surface brightness. This is even more essential for inclined debris disks seen in scattered light, since the algorithm throughput is lowest at short separations, along the inclined disks' semiminor axis where the effect of anisotropic scattering is the strongest (Hedman & Stark 2015; Perrin et al. 2015; Milli et al. 2017b). Accounting for the post-processing throughput is thus required to accurately map a disk surface brightness distribution, measure its scattering phase function (SPF) and flux density, and put constraints on its scattering properties.

In this section, we describe the parametric modeling used to constrain the disk morphologies, the forward modeling method

used to calibrate the post-processing throughput, and the models that best fit the disks detected around HD 104860 and HD 192758.

4.1. Forward Modeling Method

Assuming that the morphology of the astrophysical source is known, the post-processing throughput can be inferred though forward modeling. To constrain the morphology and photometry of the disks detected around HD 104860 and HD 192758, we used the same methodology as in Choquet et al. (2016), using parametric modeling and the analytical forward modeling method (valid with PCA-type algorithms; Soummer et al. 2012; Pueyo 2016). This method consists of subtracting from the source's model its projection on the eigenvectors used to process the data.

We generated a grid of disk models with a set of free parameters that we wish to constrain, and convolved each model with a synthetic unocculted NICMOS PSF generated in the corresponding filter with the Tiny TIM package (Krist et al. 2011). From each model, we then subtracted its projection on the same eigenvectors as used for the science data, intrinsically using the same reduction zone and number of PCs. This process removes from the raw input model the part over-subtracted during post-processing and reveals the (hereafter) forward model. We then rotated and combined these forward models with the same parameters and angles as the science images, and we scaled the resulting model to the total flux of the disk in the science image. Each forward model is then directly compared to the disk image.

We used the GRaTer radiative transfer code to create the disk models (Augereau et al. 1999b; Lebreton et al. 2012). This code computes optically thin centro-symmetric disk models assuming a Henyey & Greenstein (1941) SPF of asymmetric parameter g. The dust density distribution $n(r, z)$ is parametrized with a radial profile $R(r)$ falling off with power laws $\alpha_{\rm in}$ and $\alpha_{\rm out}$ inward and outward from a parent belt at radius R_0, and with a Gaussian vertical density $Z(r, z)$ profile with a scale height $\zeta(r)$ rising linearly with an aspect ratio h:

$$n(r, z) \propto R(r)Z(r, z), \quad (1)$$

with

$$R(r) = \left(\left(\frac{r}{R_0}\right)^{-2\alpha_{\rm in}} + \left(\frac{r}{R_0}\right)^{-2\alpha_{\rm out}}\right)^{-1/2}, \quad (2)$$

$$Z(r, z) = \exp\left(-\left(\frac{|z|}{\zeta(r)}\right)^2\right), \quad (3)$$

$$\zeta(r) = hr. \quad (4)$$

The disk center relative to the star's position is parametrized by the offsets du and dv in the disk plane, with du along the major axis (unaffected by projection effects) and dv along the perpendicular axis (appearing projected along the disk's minor axis). The model image is simulated with a PA parametrized by θ and inclination i. Given the geometry of the two systems, the vertical scale heights of the disks are not properly constrained by our data. We fix the aspect ratio to $h = 0.05$, a reasonable thickening assumption for unperturbed debris disks due to the combined action of radiation pressure and the grains' mutual collisions (Thébault 2009). Furthermore, given the inclinations of the disks, a Henyey–Greenstein SPF model will describe the surface brightness variations in the disks over a range of scattering angles limited by the disk inclinations, but it might not properly describe the actual SPF over all angles (see Hedman & Stark 2015).

Table 4
Parameter Grid and Best Model for HD 104860

Parameter	Minimum	Maximum	$N_{\rm val}$	Best Model (in grid)	Best Model (interpolated)[a]
R_0 (au)	106	122	5	114	114 ± 6
$\|g\|$	0.0	0.4	5	0.2	0.17 ± 0.13
θ (°)	−5	7	5	1	1 ± 5
i (°)	52	64	5	58	58 ± 5
$\alpha_{\rm in}$	2	10	5	10	$\geqslant 4.5$
$\alpha_{\rm out}$	−6	−2	5	−4	-3.9 ± 1.6
du (au)	−10	10	5	0	2 ± 7
dv (au)	−20	10	7	−5	-7 ± 13
$\chi^2_{\rm red}$	...	...	...	1.833	1.826

Note.
[a] Shows 1σ uncertainties.

We estimated the goodness of fit of our models to the disk image by computing the reduced $\chi^2_{\rm red}$ value over a large area encompassing the disk in the image. After identifying the best model within the grid, we refine the best-fit parameters by interpolating the reduced chi-squared values around the best model in the grid, independently for each parameter. The best chi-squared values are larger than 1 because the noise maps are overall slightly underestimated, although very representative of the noise spatial distribution (e.g., the noise signature from spider residuals). To estimate the uncertainties on the model parameters, we thus normalize the chi-squared value by its best value, assuming that the noise underestimation is common to all pixels. We then estimated the uncertainty on each parameter assuming that our estimator follows a chi-squared distribution, from the values at which the interpolated $\chi^2_{\rm red}$ increased by $1\sigma = \sqrt{2/N_{\rm dof}}$ from 1, with $N_{\rm dof}$ the number of degrees of freedom in the fit.

4.2. HD 104860 Analysis

For HD 104860, we generated a grid of 546,875 models with eight free parameters to constrain its morphology. Table 4 describes the simulated parameter ranges and best-fit values. The goodness of fit of each parameter is also presented in Figure 4. The data were fit within an elliptical area of semimajor axis 4.″2 oriented north–south and semiminor axis 2.″6, excluding the central area masked during post-processing, which resulted in $N_{\rm dof} = 5536$ degrees of freedom in the fit. This area excludes the background star ∼3.″5 from the star. The image of the best model and the comparison to the NICMOS image and noise map are presented in Figure 5 within the fit area.

We find that the best fit to HD 104860's data is a disk of radius $R_0 = 114 \pm 6$ au, inclined by $i = 58° \pm 5°$ from face-on, with a PA of $\theta = 1° \pm 5°$ east of north. These values are consistent with the morphology of the disk observed at 100 μm and 160 μm by Morales et al. (2013). We find a relatively low value for the Henyey–Greenstein parameter of anisotropic scattering, with $|g| = 0.17 \pm 0.13$, indicative of grains favoring forward scattering. This value is expected for a disk of moderate inclination such as HD 104860, which does not

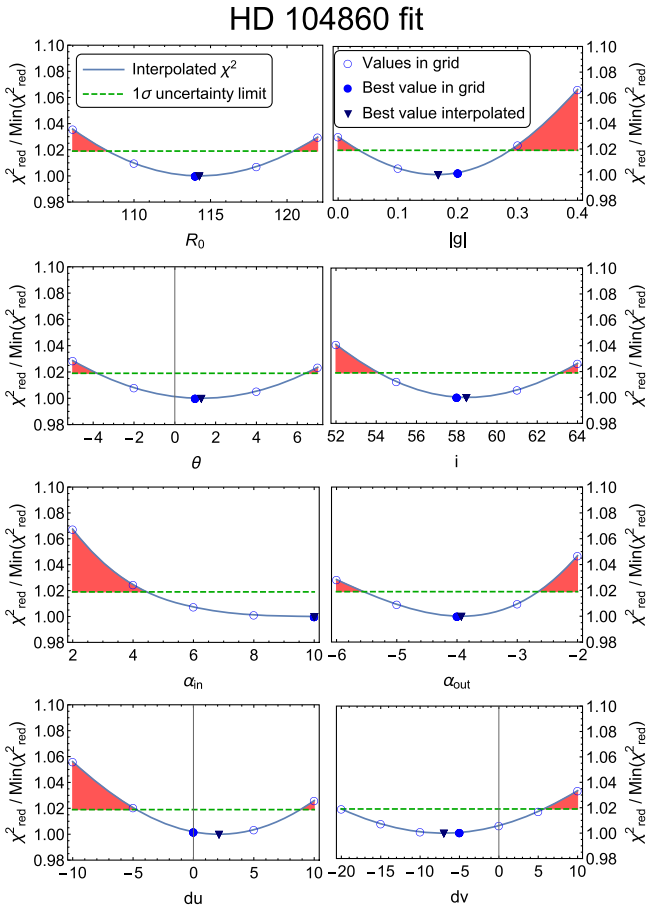

Figure 4. Goodness of fit for each parameter modeling the disk around HD 104860. The chi-squared values shown for each parameter value in the grid (empty circles) have all the other parameters fixed to their best values in the grid (filled circles). The χ^2 is interpolated between each parameter value in the grid to refine the best-fit values (filled triangles). The dashed green line shows the 1σ threshold used to estimate the uncertainties on the parameters, and the red shaded areas show the parameters values ruled out by our modeling.

probe very small scattering angles (>32°): slightly forward scattering SPFs with a Henyey–Greenstein parameter around $|g| = 0.1$–0.3 have been observed for many debris disks with similar or lower inclinations (HD 92945, HD 107146, HD 141569, HD 207129, Fomalhaut; Ardila et al. 2004; Kalas et al. 2005; Krist et al. 2010; Golimowski et al. 2011; Mawet et al. 2017). As mentioned before, this may not be representative of the SPF at smaller scattering angles, as it was shown that, for some dust grains, it may significantly differ from a Henyey–Greenstein model and sharply peak at angles below 40° despite a relatively flat phase function at large angles (Hedman & Stark 2015; Milli et al. 2017b).

Our analysis shows that the disk has a ring shape with an asymmetric radial density profile. We find that the disk outer edge follows a power law in $\alpha_{out} = -3.9 \pm 1.6$, corresponding to a surface density in $r^{\Gamma_{out}}$ with $\Gamma_{out} = \alpha_{out} + 1 = -2.9 \pm 1.6$, assuming a scale height rising linearly with radius (Augereau et al. 1999b). This is consistent within our uncertainties with disk evolution models, which predict an outer surface density profile in $\Gamma_{out} = -1.5$ for small grains created under steady-state collisions and set on eccentric orbits by radiative pressure, accumulating in the outskirts of their birth ring (Strubbe & Chiang 2006; Thébault & Wu 2008). We find that the disk inner edge is very sharp, with a lower limit of $\alpha_{in} \geqslant 4.5$ on the inward power law of its radial density profile. The sharp inner edges in debris disks can be sculpted by planets orbiting within the disk, confining the dust out of a chaotic zone through mean motion resonances (Wisdom 1980; Mustill & Wyatt 2012), while unperturbed systems have smoother inner edges filled by small grains due to Poynting–Robertson drag. We do not find significant offsets of the ring with respect to the star within ±7 au along the disk major axis, and within ±13 au projected on the minor axis, indicating that a planet responsible for carving the disk inner edge would have a low eccentricity.

Using the best-fit morphological parameter values, we deproject the NICMOS image based on the disk inclination, PA, and offsets, and compute its radial and azimuthal average profiles (see Figure 6). In the following, we quantify the disk photometry using both the NICMOS image, which is affected by oversubtraction as shown in Figure 5, and the best model before forward modeling, which is free of post-processing artifacts but is entirely model dependent.

In the NICMOS image, we measure a surface brightness on the disk spine of $11.7 \pm 0.8\,\mu$Jy arcsec^{-2} averaged over all scattering angles excluding 91° ± 23° and 271° ± 26°, where stellar residuals from the telescope spider dominate the disk brightness. We find a corresponding average surface brightness of $S = 17.8\,\mu$Jy arcsec^{-2} in the best model unbiased by oversubtraction. The south ansae is ∼30% brighter than the north one in the NICMOS image ($S_S = 16 \pm 6\,\mu$Jy arcsec^{-2} and $S_N = 12 \pm 5\,\mu$Jy arcsec^{-2} respectively), but the asymmetry is not significant given our uncertainties. From the stellar flux ($F_\star = 3.1$ Jy in the NICMOS F110W filter), we estimate that the disk has a typical reflectance of $R = S/F_\star = (5.7 \pm 0.3) \times 10^{-6}$ arcsec^{-2}, based on the mean surface brightness of the model. We estimate the disk flux density to $F_{scat} = 200 \pm 5\,\mu$Jy, integrated in the best model over an elliptical surface of 20 arcsec^2 with outer semimajor axis 3.″9, inner semimajor axis 1.″6, and the inner and outer semiminor axes projected from the semimajor axis values by the best-fit inclination cos(i), and with a PA equal to the best-fit value θ. The flux density integrated in the NICMOS image over the same surface is $92 \pm 5\,\mu$Jy, significantly affected by the post-processing throughput. Compared with the flux of the star, this correspond to a scattering efficiency of $f_{scat} = F_{scat}/F_\star = (67 \pm 2) \times 10^{-6}$, based on the model's flux density.

The scattering efficiency provides a measure of the dust-scattering albedo ω knowing the total luminosity received by the grains (Krist et al. 2010; Golimowski et al. 2011):

$$\omega = \frac{f_{scat}}{f_{emit} + f_{scat}}, \quad (5)$$

with $f_{emit} = L_{dust}/L_\star$ the disk infrared fractional luminosity. The scattering albedo is an empirical quantity that provides a degenerate, wavelength-averaged combination of the grains' albedo and of the disk SPF integrated over the scattering angles probed by the disk geometry. The true albedo of the dust can only be recovered with assumptions on the disk's SPF. Assuming that our scattering efficiency measurement integrates the light scattered by the grains responsible for the thermal emission and using the infrared fractional luminosity of $f_{emit} = 6.4 \times 10^{-4}$ reported for the outer disk by Morales

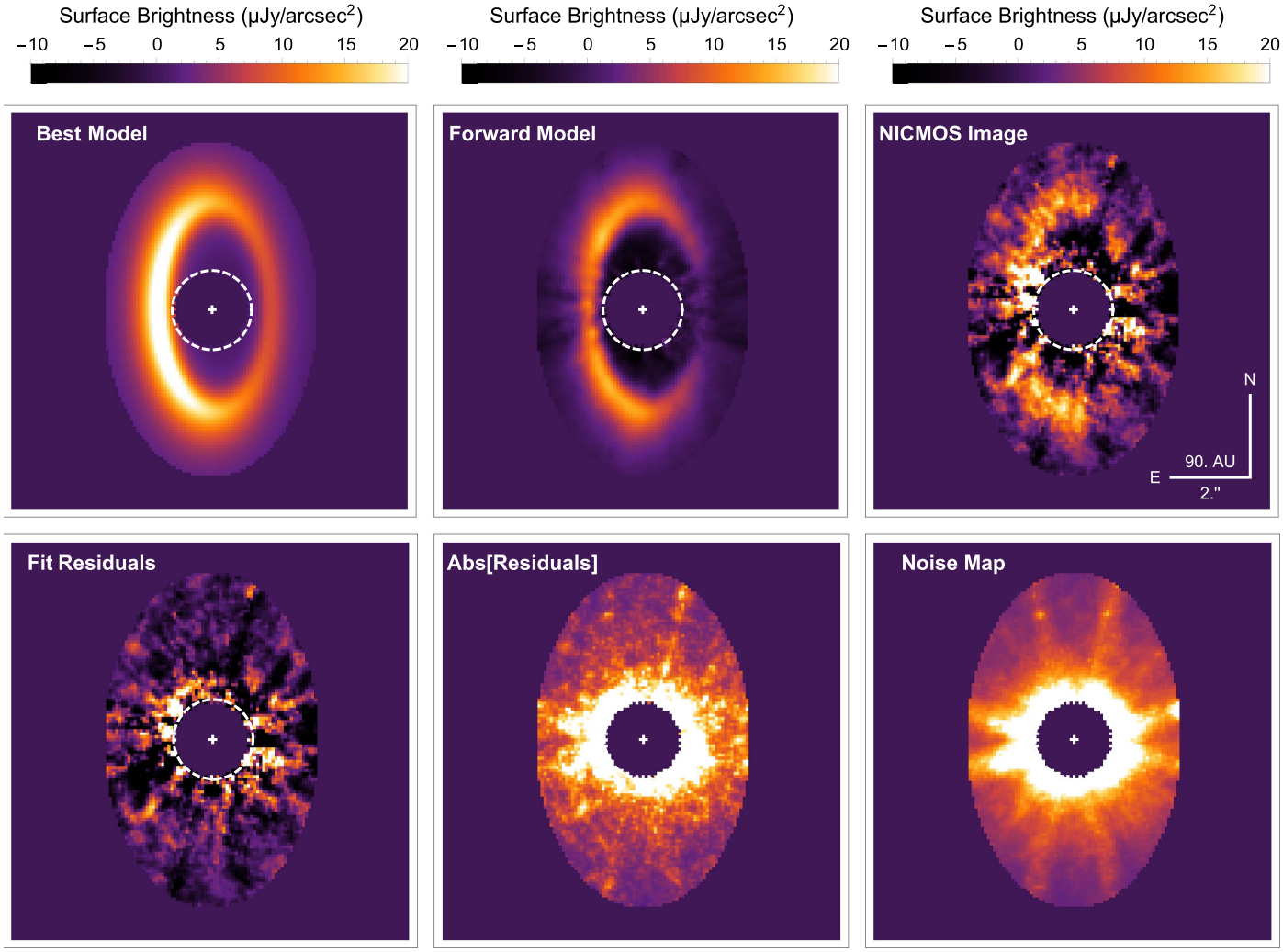

Figure 5. Best model of the debris disk detected around HD 104860. The top row shows The best raw model convolved by a NICMOS PSF (left), the model affected by oversubtraction after forward modeling (middle), and the NICMOS image for comparison (right). The bottom row shows the residuals after subtracting the forward model from the NICMOS image (left), the absolute value of these residuals (middle), and the noise map for comparison (right). No disk structure is appearing in the residual map, indicating that the model properly fits the data. All images are displayed within the elliptical mask used for the fit, and have been smoothed by convolution with a synthetic PSF. The raw model was hence convolved twice with a synthetic PSF, once to account for the diffraction and once for smoothing and comparison with the other smoothed images.

et al. (2016; well-constrained from 24 μm to 1.3 mm photometry), we find a scattering albedo of $\omega = 9.5\% \pm 0.3\%$.

We compared this value to the scattering albedo of grains with various compositions and porosities, computed under the Mie theory for a disk with the best-fit morphology found for HD 104860 in the F110W filter (Figure 7). We find that our scattering albedo estimation rules out pure water ice composition and is consistent with dirty ice grains (Preibisch et al. 1993) larger than $\sim$3 μm in the case of compact grains and larger than $\sim$1 μm in the case of 90% porous grains. Assuming compact grains, this is consistent with particles larger than the blowout size, as was suggested by Pawellek et al. (2014) for this disk (typical grain size of 7 μm, blowout size of 0.4 μm), although they used pure silicate grains in their study. Assuming 90% porous grains, the blowout size is 10 times larger than that for compact grains, which is consistent with our scattering albedo value. A few other debris disks, e.g., HD 181327 and HD 32297, are suspected to have porous grains (Lebreton et al. 2012; Donaldson et al. 2013). However, they are also much brighter than HD 104860, which may also indicate a different composition.

4.3. HD 192758 Analysis

For HD 192758, we generated a single grid of models that we fit separately to the F110W and F160W images. It is indeed reasonable to assume a similar dust density distribution in both images but possibly different scattering properties at the two different wavelengths (albedo, SPF). We simulated 604,800 models with seven free parameters, fixing the offset along the disk minor axis to $dv = 0$, as this parameter is unconstrained by our data given the disk geometry. We present the simulated parameter ranges and best-fit values in Table 5 for both filters. The goodnesses of fit are presented jointly in Figure 8. The shaded areas show better constraints on some parameters when combining the fits to both data sets. We computed the chi-squared values in an elliptical area of semimajor axis 2.″6 oriented east–west and semiminor axis 1.″9, and excluding the central area masked during post-processing. The same area was used for both

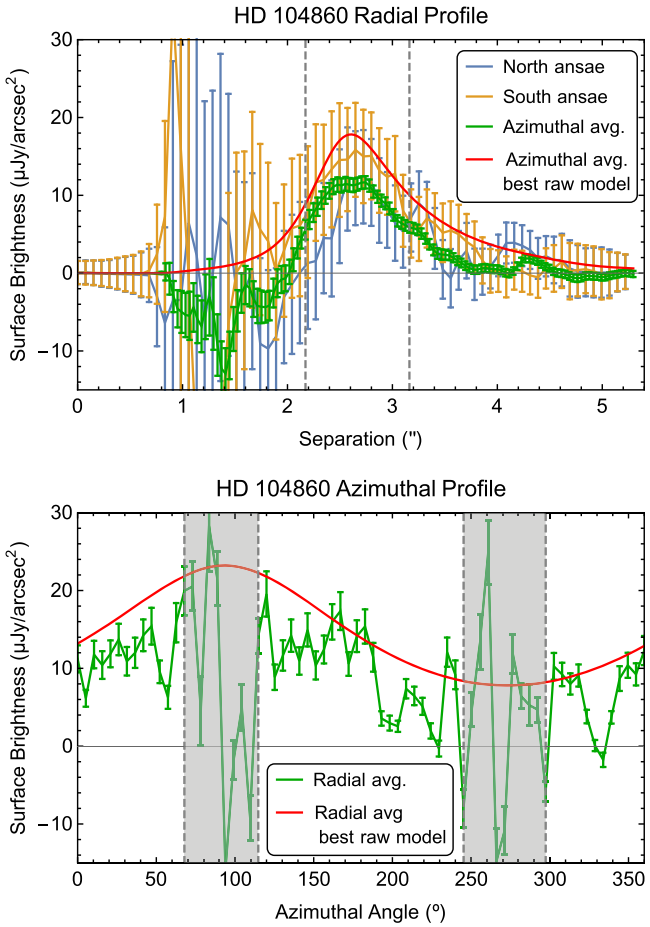

Figure 6. Radial and azimuthal profiles of HD 104860, measured after deprojecting the disk from its inclination, position angle, and offset from the star. Top: the blue and orange lines show the disk profile in the north and south ansae, respectively. The green line shows the radial profile averaged regardless of the anisotropy of scattering over all azimuthal angles (excluding the angles around 90° and 270° delimited by the gray dashed lines in the bottom plot). All three profiles are affected by the oversubtraction induced by post-processing. The red line shows the average radial profile measured in the best raw model, before forward modeling, and is representative of the disk surface brightness unaffected by oversubtraction artifacts. The dashed gray lines show the disk's FWHM. Bottom: azimuthal profile of the disk average over the disk's FWHM (green line). The red line shows the average azimuthal profile of the best model before forward modeling, and corresponds to a Henyey–Greenstein SPF of parameter $g = 0.17$. The dashed gray lines show the azimuthal angles where the disk is dominated by PSF residuals, along the minor axis at 90° and 270°. The 1σ uncertainties are computed accordingly from the noise map.

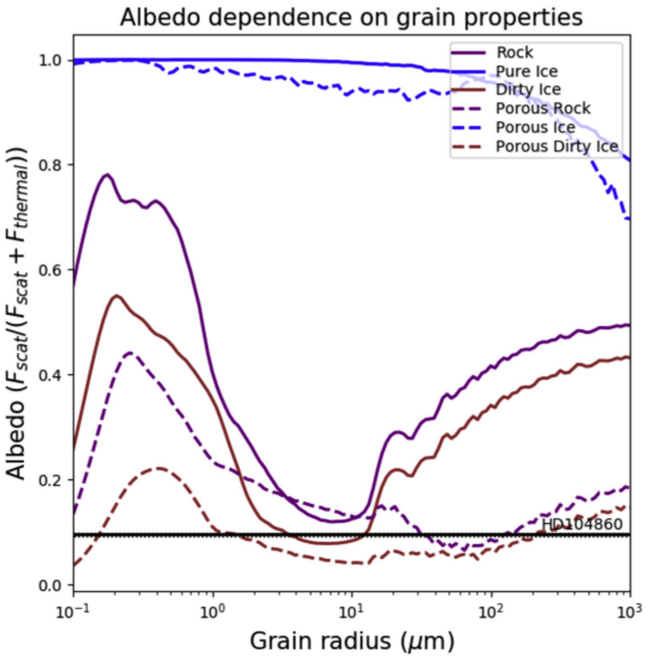

Figure 7. Scattering albedo computed under the Mie theory as a function of grain size for a disk with HD 104860's best-fit morphology, assuming different grain compositions—pure ice (blue), dirty ice (red), silicates (purple)—and different porosities—compact grains (solid lines) and 90% porous grains (dashed lines). The measured scattering albedo for HD 104860 (black line) rules out water ice compositions and is consistent with dirty ice grains larger than ~ 2 μm.

data sets and corresponds to $N_{\rm dof} = 2525$ degrees of freedom. We show in Figure 9 the best fit to the F110W data set and in Figure 10 the best fit to the F160W data, along with their respective comparison to the NICMOS images and noise maps.

We find that the best-fit parameters are consistent for both data sets. In the following, we describe the best model by averaging the F110W and F160W best parameter values and the uncertainties combined from the two fits, which provides better constraints, except for two parameters ($|g|$ and θ) as discussed below. The disk has a radius of $R_0 = 95 \pm 9$ au and is seen inclined by $i = 59° \pm 7°$ from face-on. The best-fit PA differs by 8° between the two data sets. This may be due to starlight residuals from the telescope spider, at a comparable orientation to the disk major axis, which may bias the disk PA. The mean PA between both fits is $\theta = -89° \pm 12°$ east of north, using conservative error bars encompassing uncertainties from the two fits. The disk has a relatively low Henyey–Greenstein parameter of anisotropic scattering, with values of $|g| = 0.29 \pm 0.12$ in the F110W image and $|g| = 0.41 \pm 0.16$ in the F160W image. Differing values can be explained by different scattering properties at different wavelengths, although we do not expect a significant difference, as the two bandpasses are relatively close. As for HD 104860, these relatively low values are consistent with the finding of Hedman & Stark (2015) about the apparently low g values of inclined disks observed only near scattering angles of 90°.

We find that the dust density follows a radial power law in $\alpha_{\rm out} = -2 \pm 0.8$ outward from the parent radius, which is very consistent with the sharpness expected from evolution models with small grains on eccentric orbits accumulating outside of the main belt colliding zone (Thébault & Wu 2008). Given the disk inclination and the quality of our images, we can only put a weak constraint on the radial profile inward from the parent radius R_0, with a power-law coefficient steeper than $\alpha_{\rm in} > 2.9$. We find that the disk center may be offset by $du = 7 \pm 12$ au along the major axis but we cannot rule out a system centered with the star.

As shown in Figures 9 and 10, oversubtraction from post-processing strongly affects the disk photometry, due to its compact appearance in the image (1.″4 semimajor axis, and 0.″7 semiminor axis at the edge of the reduction mask). The averaged radial and azimuthal profiles measured in the NICMOS images are thus noisy and biased by oversubtraction so we relate hereafter photometric values from the best models before forward modeling only. In the F110W filter, we measure a mean surface brightness of $S^{\rm F110W} = 108 \pm 3$ μJy arcsec^{-2} in the north ansae and $S^{\rm F160W} = 81 \pm 5$ μJy arcsec^{-2} in the F160W data. Given the stellar flux in these bands ($F_\star^{\rm F110W} = 4.85$ Jy and $F_\star^{\rm F160W} = 3.26$ Jy, respectively), the disk reflectances in the north ansae

Table 5
Parameter Grid and Best Models for HD 192758

Parameter	Minimum	Maximum	N_{val}	F110W Best Model (in grid)	F110W Best Model (interpolated)[a]	F160W Best Model (in grid)	F160W Best Model (interpolated)[a]
R_0 (au)	81	109	5	95	95 ± 12	95	95 ± 9
$\|g\|$	0.15	0.6	10	0.3	0.29 ± 0.12	0.4	0.41 ± 0.16
θ (°)	−101	−77	7	−93	-93 ± 7	−85	-85 ± 8
i (°)	50	70	6	62	60 ± 8	58	58 ± 7
α_{in}	1	11	6	7	$\geqslant 1.4$	11	$\geqslant 2.9$
α_{out}	−3.5	−1	6	−2	-2.0 ± 0.8	−2	-2.0 ± 0.9
du (au)	−10	25	8	10	11 ± 15	5	4 ± 12
χ^2_{red}	...	...	...	4.864	4.857	2.247	2.246

Note.
[a] Shows 1σ uncertainties.

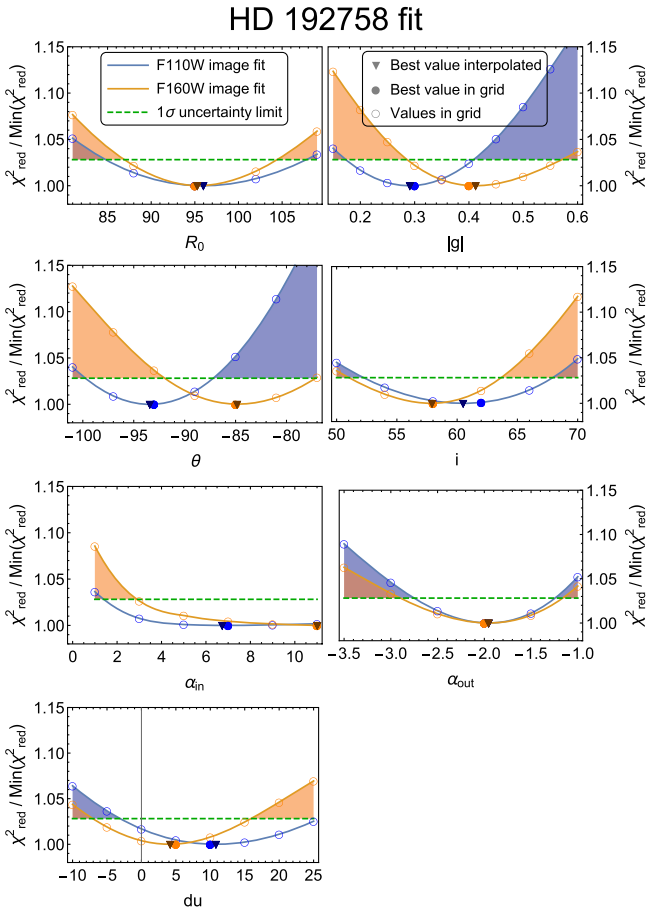

Figure 8. Goodness of fit for each parameter for the disk around HD 192758, in blue for the F110W filter data set and in orange for the F160W data set. The chi-squared values shown for each value in the grid (empty circles) have all the other parameters fixed to their best values in the grid (filled circles). The χ^2 is interpolated between each parameter value in the grid to refine the best-fit values (filled triangles). The dashed green line shows the 1σ threshold used to estimate the uncertainties. The shaded areas show the parameter values ruled out by our modeling.

are $R^{F110W} = (22.3 \pm 0.6) \times 10^{-6}$ arcsec^{-2} and $R^{F160W} = (25 \pm 2) \times 10^{-6}$ arcsec^{-2} in the F110W and F160W NICMOS filters. By integrating the disk flux over a 7.1 arcsec^2 elliptical area (outer and inner semimajor axes $2\farcs3$ and $1\farcs0$, oriented with the best PA θ east of north, minor axes projected by $\cos(i)$ from the major axis values), we find flux densities of $F_{scat}^{F110W} = 411 \pm 9$ μJy in the F110W filter and $F_{scat}^{F160W} = 319 \pm 12$ μJy in the F160W filter. After normalizing by the stellar contribution, we find that the disk around HD 192758 has scattering efficiencies of $f_{scat}^{F110W} = (85 \pm 2) \times 10^{-6}$ and $f_{scat}^{F160W} = (98 \pm 4) \times 10^{-6}$, respectively, in the two NICMOS filters.

From these scattering efficiency measurements in two different NICMOS filters, we can measure the disk color. We find that it has a scattering efficiency ratio of $f_{scat}^{F110W}/f_{scat}^{F160W} = 0.87 \pm 0.05$ (F110W – F160W color index of 0.15), indicating a red color for the disk. Assuming spherical silicate grains following the Mie theory, this color is consistent with the lack of particles smaller than $\sim$0.5 μm in the parent belt, which is also consistent with the minimum size $a_{blow} = 1.4$ μm under which silicate grains are blown out from the system by radiative pressure, assuming a stellar luminosity $L = 4.9\,L_\odot$, stellar mass of $M = 1.2\,M_\odot$, and a dust mass density of $\rho = 3.3$ g.cm^{-3}.

Based on the disk infrared fractional luminosity $f_{emit} = (5.7 \pm 0.3) \times 10^{-4}$ from Moór et al. (2011), we find scattering albedo values of $\omega^{F110W} = 13.0\% \pm 0.6\%$ and $\omega^{F160W} = 14.7\% \pm 0.7\%$ in the F110W and F160W filters, respectively. As found for HD 104860, these values rule out pure water ice composition (see Figure 11). They are consistent with compact silicate grains larger than $\sim$6 μm, which is significantly larger than the blowout size of $a_{blow} = 1.4$ μm for this system, as well as with dirty ice grains larger than $\sim$3 μm.

5. Discussion

These two detections add to a growing population of debris disks resolved in scattered light. To date, 41 of such have been imaged around stars from $\sim$10 Myr to a few Gyr, over a large range of spectral types (See Figure 1). Yet, considering the numerous attempts to image debris disks around systems with large infrared excess indicative of a massive dust belt presumably detectable with basic geometric and albedo assumptions, this remains a relatively low number of detections. Three reasons could explain the non-detections, given that the these surveys were designed to reach surface brightness limits based on assumptions on the disk radii and albedos.

1. *Inaccurate radius estimations*: radius estimations based solely on the blackbody fit of SEDs are known to be degenerate with the dust size distribution and can be very inaccurate. The missed disks may have radii different

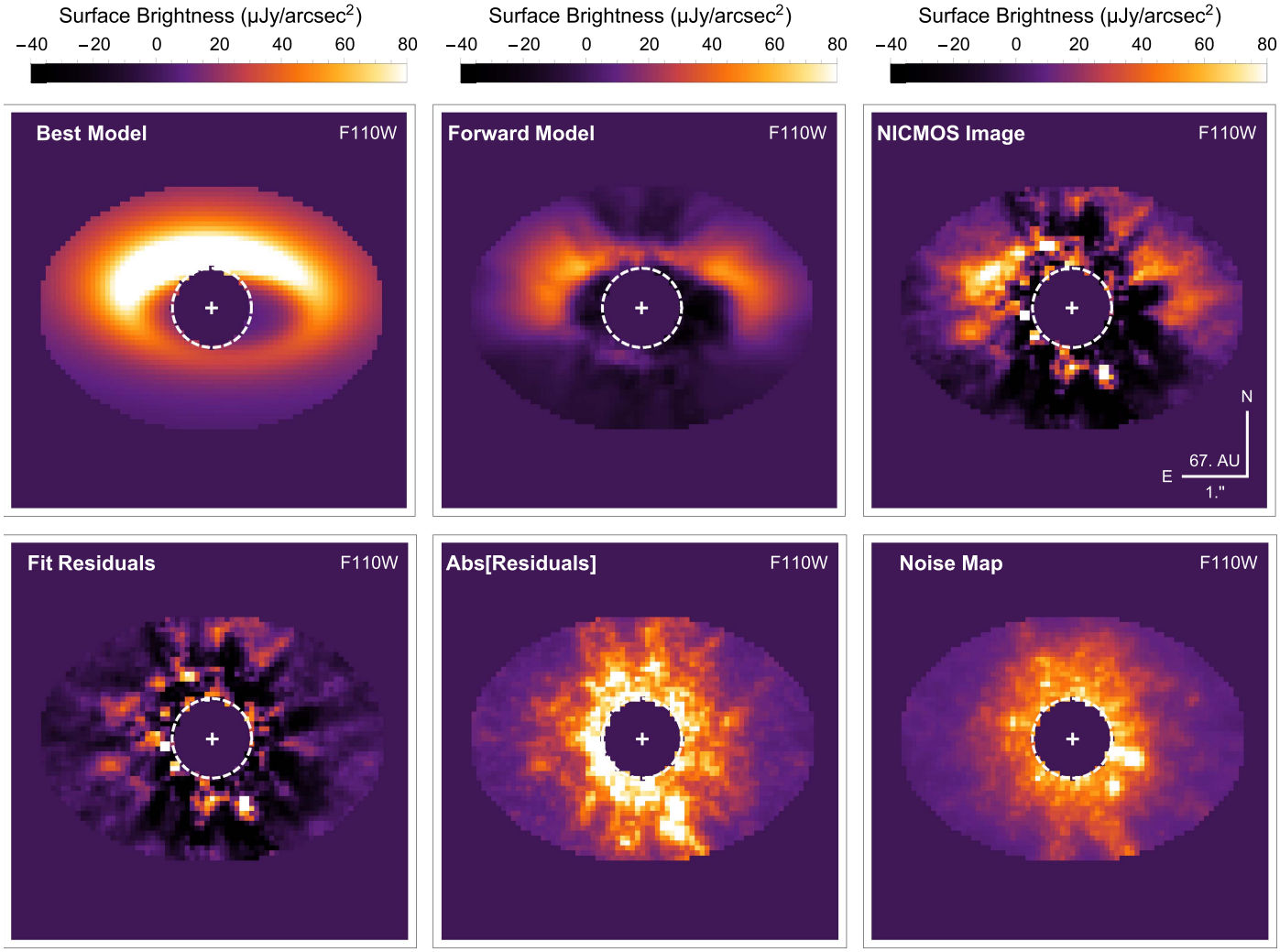

Figure 9. Same as Figure 5 for HD 192758 in the F110W filter.

from those inferred from SED modeling by a factor of 0.5 to 2. They could either be too compact to be observable with the $\sim 0\farcs3$ typical inner working angle (IWA) of current coronagraphic instruments, or be larger and thus fainter than expected, falling short of the sensitivity limits planned for these surveys.

2. *Simplistic SPF assumptions:* exposure times assuming isotropic scattering may have been underestimated if the disks have more complex SPFs, depending on their inclination to our line of sight. Recent work showed that the minimum grain sizes estimated by SED modeling are often several microns and much larger than the blowout size (Pawellek & Krivov 2015), which suggest that wrong estimations may have been used on the grain size distribution and SPF in older surveys. Furthermore, low-inclination disks not only appear fainter than expected if their SPF peaks at unprobed scattering angles, but they are also harder to detect with most post-processing techniques: they are self-subtracted with ADI-based algorithms, and oversubtracted with RDI-based techniques.
3. *Unexpectedly low albedos*: the undetected disks may have dust compositions with albedo lower than what we expect from basic assumptions (e.g., water ice, Mie theory, etc.), and than what we observed for the bright disks well-characterized so far.

We should also mention the possibility of chance non-detection, due to azimuthal sensitivity variations (telescope spider) or azimuthal coverage of the instruments (*HST* STIS wedge), e.g., the detection of the edge-on disk around HD 377 with NICMOS (Choquet et al. 2016), but non-detection with STIS due to chance alignment with the wedge and with the telescope spider (Krist et al. 2012). Such unlucky configurations cannot explain the statistical trend seen in the different surveys with both ground-based telescopes and *HST* though.

The new generation of high-contrast imaging instruments on ground-based telescopes with extreme adaptive optics systems now offers smaller IWAs, opening the detection space toward more compact disks. Yet, only a handful of new debris disks have been detected with these instruments so far. These detections have been made possible by improved sensitivity limits at large separation compared to the first generation of imagers, rather than by smaller IWAs (e.g., HD 131835, HD 206893; Hung et al. 2015; Milli et al. 2017a). Similarly, by pushing the sensitivity limits on *HST*-NICMOS data with modern post-processing techniques, we have discovered 11 debris disks, 10 of which with very low surface brightnesses from a few 100 μJy arcsec^{-2} (Soummer et al. 2014; Choquet

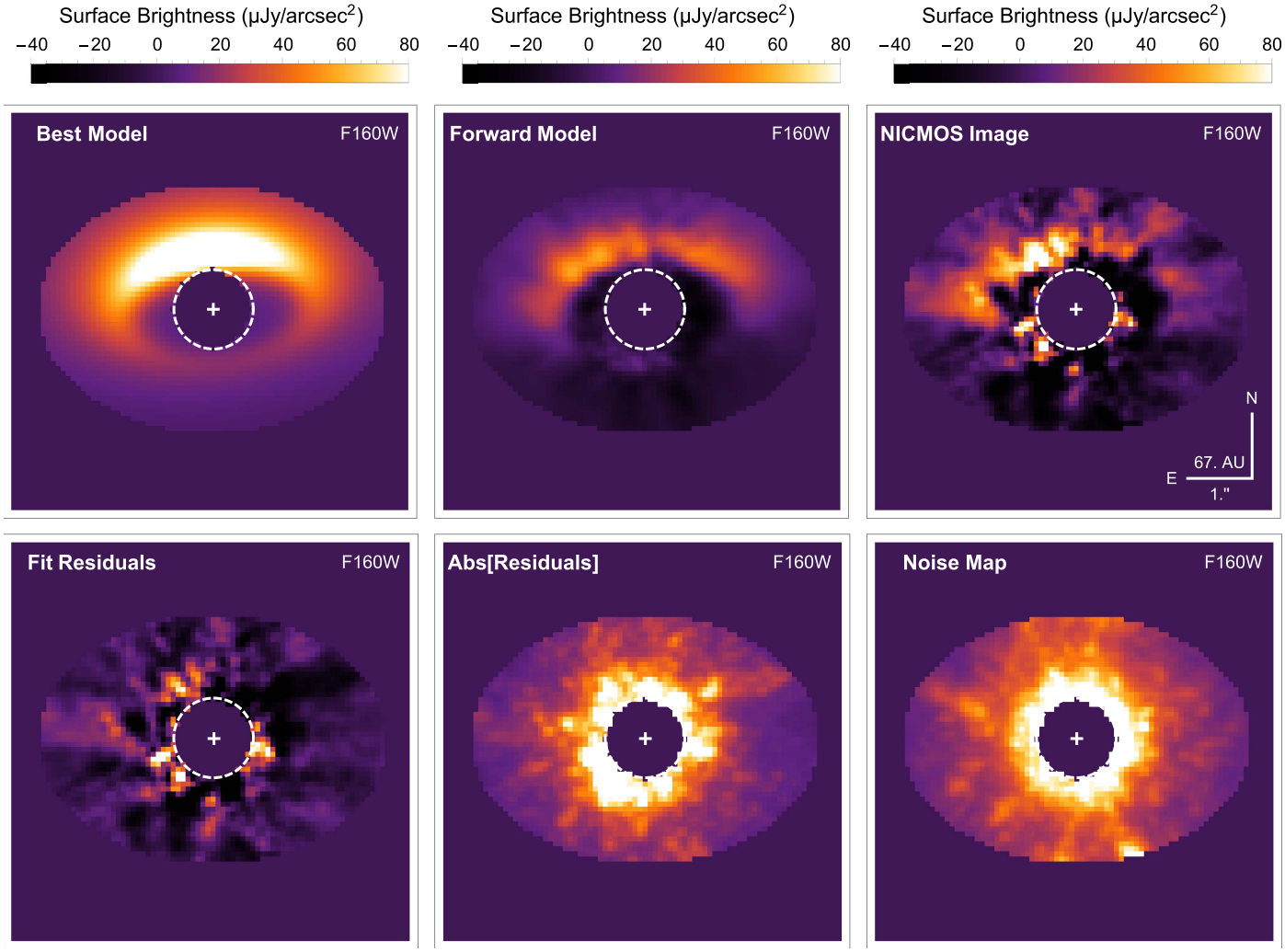

Figure 10. Same as Figure 5 for HD 192758 in the F160W filter.

et al. 2017) down to a few 10 μJy arcsec^{-2}, including these two around HD 104860 and HD 192758 (Choquet et al. 2016; this work). These combined results seem to indicate that there is an underlying population of debris disks much fainter than the population of bright debris disks discovered so far, indicative of low scattering albedos. A rigorous statistical analysis estimating the completeness of previous surveys to debris disks as a function of their morphology is required to assess the properties of debris disks as a whole population. Such a study is out of the scope of the present paper though, and we only discuss below comparisons with previously detected systems.

The disks observed around HD 104860 and HD 192758 share several common properties. They have very similar fractional infrared luminosities ($\sim 6 \times 10^{-4}$) and are seen with the same inclination of $\sim 60°$, which makes their scattering properties directly comparable. In particular, these two disks appear very faint in scattered light, having peak surface brightnesses of a few tens of μJy arcsec^{-2} only, and have low scattering albedo values (10%–15%). A few other systems with similar inclinations also have comparably low scattering albedo values: HD 92945, HD 207129, HD 202628, and Fomalhaut (Kalas et al. 2005; Krist et al. 2010, 2012; Golimowski et al. 2011, respectively). Table 6 reports the properties of debris disks with inclinations in the 50°–70° range with published scattering albedo values estimated with Equation (5) or with published scattering efficiencies. There are two populations of debris disks with distinct dust compositions, leading to low albedo values around 5%–15% for one population, and higher albedos around 50%–70% for the other. This distinction seems independent from the age of the system or the mass of the host star. Although the sample is incomplete, these populations with distinct albedos seem to be present in other inclinations ranges, e.g., HD 107146 and HD 181327 in the 20°–30° range with scattering albedos of 15% and 65%, respectively (Chen et al. 2014; Schneider et al. 2014), or HD 139664 and HD 61005 in the 80°–90° bin with respective scattering albedos of 9% and 64% (Chen et al. 2014; Schneider et al. 2014).

Interestingly, the majority of comets in the solar system display low albedos of 4%–5% in the visible (Kolokolova et al. 2004) that can be well reproduced by mixtures of both submicron aggregates and compact particles (Kolokolova & Kimura 2010). On the other hand, infrared observations of the coma of the pristine Oort Cloud comet C/2012 K1 (Pan-STARRS) are well modeled by compact, carbon-dominated grains, while it also displays a low albedo of 14% ± 0.01% at a scattering angle of $\sim 35°$ at infrared wavelengths (8–31 μm), comparable with the values that we measure for HD 104860 and HD 192758 in the near-infrared (Woodward et al. 2015). This scattering angle, set by the position of the comet with respect to the Sun and the SOFIA telescope at the moment of the

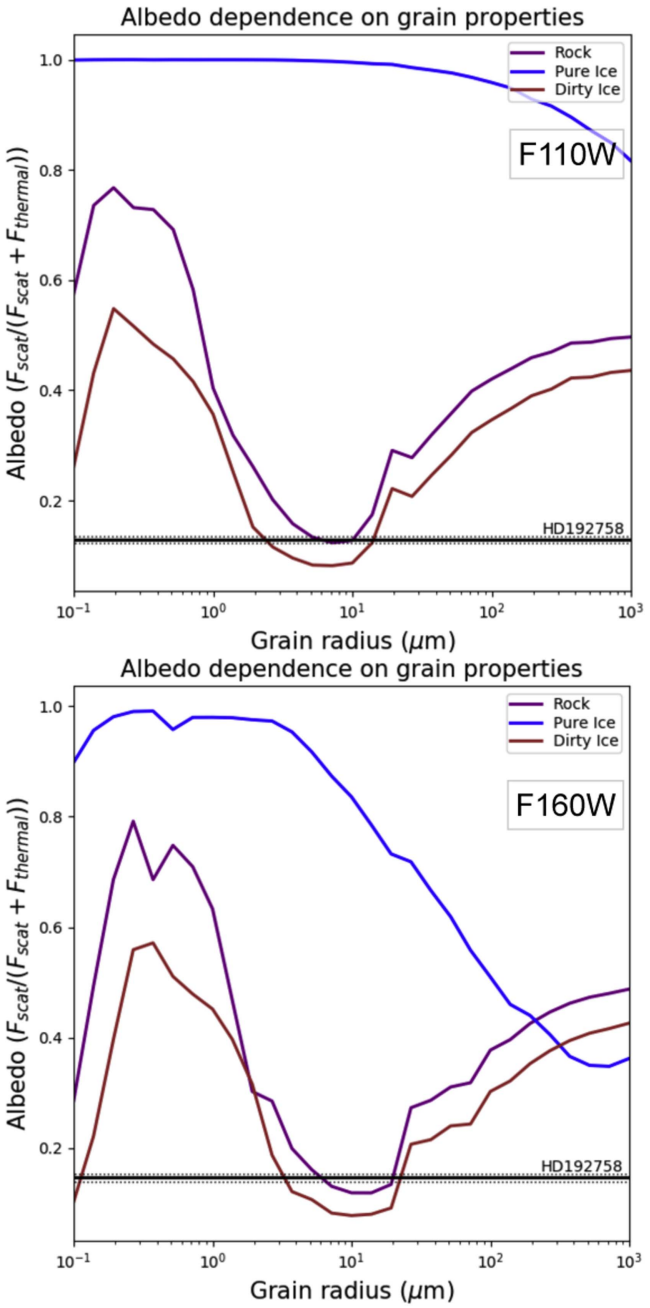

Figure 11. Scattering albedo as a function of grain size for a disk with HD 192758's best-fit morphology, assuming different grain compositions—pure ice (blue), dirty ice (purple), silicates (red)—and computed in the F110W filter (top) and F160W filter (bottom). The measured scattering albedo for HD 192758 (black line) rules out pure water ice compositions and is consistent with dirty ice grains larger than $\sim$3 μm and pure silicate grains larger than $\sim$6 μm.

Table 6
Scattering Albedos of $\sim$60° Inclination Debris Disks

System	Spectral Type	Age (Myr)	Inc. (°)	Scattering Albedo	λ (μm)	References
HD 202628	G5	2300	64	0.05	0.5	1
Fomalhaut	A4	440	66	0.05	0.8	2
HD 207129	G0	2100	60	0.06	0.6	3
HD 92945	K1	294	62	0.09	0.5	4, 5
				0.10	0.6	6
HD 104860	F8	32	58	0.10	1.1	8
HD 192758	F0	830	59	0.13	1.1	8
HD 202917	G7	45	69	0.50	0.5	7
HD 15745	F2	23	67	0.63	0.5	4, 5

References. (1) Krist et al. (2012), (2) Kalas et al. (2005), (3) Krist et al. (2010), (4) Schneider et al. (2014), (5) Chen et al. (2014), (6) Golimowski et al. (2011), (7) Schneider et al. (2016), (8) this work.

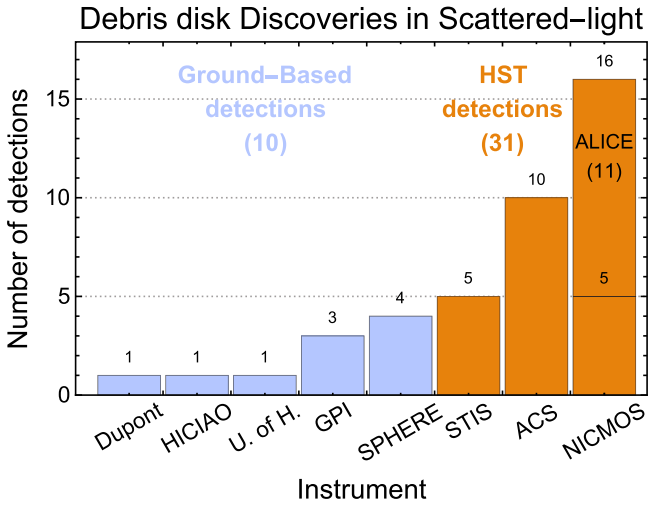

Figure 12. Number of debris disks imaged for the first time in scattered light per instrument. The ground-based instruments are highlighted in blue (total of 10 discoveries to date), and the *HST* instruments are highlighted in orange (31 discoveries to date). The NICMOS detections are split between pre-ALICE disks (5 detections) and ALICE disks (11 detections). References—Dupont 2.5 m telescope: Smith & Terrile (1984); Subaru-HICIAO: Thalmann et al. (2013); University of Hawaii 2.2 m telescope: Kalas et al. (2004); Gemini-GPI: Hung et al. (2015), Currie et al. (2015), Kalas et al. (2015); VLT-SPHERE: Kasper et al. (2015), Wahhaj et al. (2016), Matthews et al. (2017), Milli et al. (2017a); *HST*-STIS: Krist et al. (2012), Padgett & Stapelfeldt (2016); *HST*-ACS: Ardila et al. (2004), Kalas et al. (2005, 2006, 2007a, 2007b), Krist et al. (2010), Golimowski et al. (2011), and two unpublished detections presented at conferences: HD 10647 (Stapelfeldt et al. 2007), HD 202917 (Krist 2007); *HST*-NICMOS: Weinberger et al. (1999), Augereau et al. (1999a), Schneider et al. (1999, 2005); Schneider et al. (2006), Hines et al. (2007), Soummer et al. (2014), Choquet et al. (2016, 2017), this work.

observations, is at the limit of the minimum scattering angles probed in these two disks. These examples indicate that low-albedo dust is common in the solar solar system and can be explained by solid grains, or by submicron aggregates, or by mixtures of both. Identifying the reason for the low-albedo values in debris disks systems cannot be achieved without combining resolved observations in several wavelengths regimes. Different albedo values can indeed be explained not only by dust porosity but also by different chemical compositions or by different dust size distributions. In the former case, this may indicate different initial conditions or formation mechanisms in the primordial disk that would generate planetesimals with different compositions. In the latter case, different dust size distributions would indicate different dynamical mechanisms at work after the transition from the protoplanetary stage to the evolved stage of debris disks. A better characterization of these systems would be needed to discriminate one scenario from the other, for instance by constraining their dust size distribution with multiband imaging.

6. Conclusion

To conclude, we have detected two debris disks in scattered light, around HD 104860 and HD 192758. The former disk has previously been imaged in thermal emission with *Herschel* but never in scattered light, and the latter disk has never been imaged before. These disks were found in archival *HST*-NICMOS data in the near-infrared, from our reanalysis using modern PSF subtraction techniques as part of the ALICE project. These two detections bring the number of debris disks discovered in scattered light by this program to 11, and make NICMOS the instrument with the largest number of debris disk imaged in this regime to date (see Figure 12).

We carefully characterized the morphology of these disks with forward modeling techniques in order to calibrate the post-processing artifacts. The disk around HD 104860 has a well-defined ring shape with sharp edges at a radius of 114 au. The slope of the outer edge is consistent with evolution models, and the sharp inner edge is likely sculpted by an unseen planet through secular resonances. Planets of a few Earth masses with small eccentricities can cause such ring shapes in debris disk systems (Lee & Chiang 2016). The disk around HD 192758 has a radius of 95 au. Both disks are inclined by $\sim 60^\circ$ from face-on, and have very low albedo values of 10% and 13% respectively, which exclude compositions of pure water ice.

They are reminiscent of several other disks previously detected with *HST* showing similarly low albedo values, around Fomalhaut, HD 202628, HD 207129, and HD 92945. These disks may have similar dust compositions, differing from the many brighter disks that have been imaged thus far in scattered light. Interestingly, comets in solar systems also display comparably low albedo values in the visible. Porous grains, chemical composition, as well as different dust size distributions may explain the differences in albedo in the observed populations of disks. A better characterization of these systems with images in complementary bandpasses would help us understand the different properties between these systems.

E.C. acknowledges support from NASA through Hubble Fellowship grant HF2-51355 awarded by STScI, which is operated by AURA, Inc. for NASA under contract NAS5-26555, for research carried out at the Jet Propulsion Laboratory, California Institute of Technology. J.-C.A. acknowledges support from the "Programme National de Planétologie" (PNP) of CNRS/INSU co-funded by the CNES. This work is based on data reprocessed as part of the ALICE program, which was supported by NASA through grants HST-AR-12652 (PI: R. Soummer), HST-GO-11136 (PI: D. Golimowski), HST-GO-13855 (PI: E. Choquet), HST-GO-13331 (PI: L. Pueyo), and STScI Director's Discretionary Research funds. Part of these data were calibrated as part of the LAPLACE program, which was supported by NASA through grants HST-AR-11279 (PI: G. Schneider). This research has made use of NASA's Astrophysics Data System (ADS), the Washington Double Star Catalog, maintained at the U.S. Naval Observatory, the Keck Observatory Archive (KOA), operated by the W. M. Keck Observatory and the NASA Exoplanet Science Institute (NExScI) under contract with NASA, the SIMBAD database, operated at CDS, Strasbourg, France, and of data from the European Space Agency (ESA) mission *Gaia*. This research has used archival data from *HST* programs HST-GO-10527 (PI: D. Hines) and HST-GO-11157 (PI: J. Rhee), and from Keck programs. We thank the anonymous referee for comments which made the paper much clearer.

Facility: HST(NICMOS).

ORCID iDs

É. Choquet https://orcid.org/0000-0002-9173-0740
M. D. Perrin https://orcid.org/0000-0002-3191-8151
R. Soummer https://orcid.org/0000-0003-2753-2819
C. H. Chen https://orcid.org/0000-0002-8382-0447
J. H. Debes https://orcid.org/0000-0002-1783-8817
D. C. Hines https://orcid.org/0000-0003-4653-6161
D. Mawet https://orcid.org/0000-0002-8895-4735
F. Morales https://orcid.org/0000-0001-9414-3851
B. Ren https://orcid.org/0000-0003-1698-9696
G. Schneider https://orcid.org/0000-0002-4511-5966

References

Ardila, D. R., Golimowski, D. A., Krist, J. E., et al. 2004, ApJL, 617, L147
Augereau, J. C., Lagrange, A. M., Mouillet, D., & Ménard, F. 1999a, A&A, 350, L51
Augereau, J. C., Lagrange, A. M., Mouillet, D., Papaloizou, J. C. B., & Grorod, P. A. 1999b, A&A, 348, 557
Barrado y Navascués, D., Stauffer, J. R., & Jayawardhana, R. 2004, ApJ, 614, 386
Booth, M., Dent, W. R. F., Jordán, A., et al. 2017, MNRAS, 469, 3200
Booth, M., Jordán, A., Casassus, S., et al. 2016, MNRAS, 460, L10
Booth, M., Kennedy, G., Sibthorpe, B., et al. 2013, MNRAS, 428, 1263
Brandt, T. D., McElwain, M. W., Turner, E. L., et al. 2014, ApJ, 794, 159
Chen, C. H., Mittal, T., Kuchner, M., et al. 2014, ApJS, 211, 25
Choquet, É., Milli, J., Wahhaj, Z., et al. 2017, ApJL, 834, L12
Choquet, É., Pueyo, L., Hagan, J. B., et al. 2014, Proc. SPIE, 9143, 57
Choquet, É., Perrin, M. D., Chen, C. H., et al. 2016, ApJL, 817, L2
Currie, T., Lisse, C. M., Kuchner, M., et al. 2015, ApJL, 807, L7
Cutri, R. M., Skrutskie, M. F., van Dyk, S., et al. 2003, yCat, 2246, 0
Dohnanyi, J. S. 1969, JGR, 74, 2531
Donaldson, J. K., Lebreton, J., Roberge, A., Augereau, J.-C., & Krivov, A. V. 2013, ApJ, 772, 17
Draine, B. T. 2003, ARA&A, 41, 241
Eiroa, C., Marshall, J. P., Mora, A., et al. 2013, A&A, 555, A11
Gaia Collaboration, Brown, A. G. A., Vallenari, A., et al. 2016, A&A, 595, A2
Gáspár, A., Psaltis, D., Rieke, G. H., & Özel, F. 2012, ApJ, 754, 74
Golimowski, D. A., Krist, J. E., Stapelfeldt, K. R., et al. 2011, AJ, 142, 30
Hagan, J. B., Choquet, E., Soummer, R., & Vigan, A. 2018, AJ, submitted
Hedman, M. M., & Stark, C. C. 2015, ApJ, 811, 67
Henyey, L. G., & Greenstein, J. L. 1941, ApJ, 93, 70
Hillenbrand, L. A., Carpenter, J. M., Kim, J. S., et al. 2008, ApJ, 677, 630
Hines, D. C., Schneider, G., Hollenbach, D., et al. 2007, ApJL, 671, L165
Holland, W. S., Matthews, B. C., Kennedy, G. M., et al. 2017, MNRAS, 470, 3606
Hung, L.-W., Duchêne, G., Arriaga, P., et al. 2015, ApJL, 815, L14
Kalas, P., Duchene, G., Fitzgerald, M. P., & Graham, J. R. 2007a, ApJL, 671, L161
Kalas, P., Fitzgerald, M. P., & Graham, J. R. 2007b, ApJL, 661, L85
Kalas, P., Graham, J. R., & Clampin, M. 2005, Natur, 435, 1067
Kalas, P., Graham, J. R., Clampin, M. C., & Fitzgerald, M. P. 2006, ApJL, 637, L57
Kalas, P., Liu, M. C., & Matthews, B. C. 2004, Sci, 303, 1990
Kalas, P. G., Rajan, A., Wang, J. J., et al. 2015, ApJ, 814, 32
Kasper, M., Apai, D., Wagner, K., & Robberto, M. 2015, ApJL, 812, L33
Kolokolova, L., Hanner, M. S., Levasseur-Regourd, A.-C., & Gustafson, B. Å. S. 2004, in Comets II, ed. M. C. Festou, H. U. Keller, & H. A. Weaver (Tucson, AZ: Univ. Arizona Press), 577
Kolokolova, L., & Kimura, H. 2010, EP&S, 62, 17
Krist, J. 2007, In the Spirit of Bernard Lyot: The Direct Detection of Planets and Circumstellar Disks in the 21st Century, ed. P. Kalas (Berkeley, CA: Univ. California), 32
Krist, J. E., Hook, R. N., & Stoehr, F. 2011, Proc. SPIE, 8127, 81270j
Krist, J. E., Stapelfeldt, K. R., Bryden, G., et al. 2010, AJ, 140, 1051
Krist, J. E., Stapelfeldt, K. R., Bryden, G., & Plavchan, P. 2012, AJ, 144, 45
Krivov, A. V. 2010, RAA, 10, 383

Lafrenière, D., Marois, C., Doyon, R., Nadeau, D., & Artigau, É. 2007, ApJ, 660, 770
Lebreton, J., Augereau, J.-C., Thi, W.-F., et al. 2012, A&A, 539, A17
Lee, E. J., & Chiang, E. 2016, ApJ, 827, 125
Lowrance, P. J., McCarthy, C., Becklin, E. E., et al. 1999, ApJL, 512, L69
MacGregor, M. A., Lawler, S. M., Wilner, D. J., et al. 2016a, ApJ, 828, 113
MacGregor, M. A., Matrà, L., Kalas, P., et al. 2017, ApJ, 842, 8
MacGregor, M. A., Wilner, D. J., Chandler, C., et al. 2016b, ApJ, 823, 79
MacGregor, M. A., Wilner, D. J., Rosenfeld, K. A., et al. 2013, ApJL, 762, L21
Marois, C., Lafrenière, D., Doyon, R., Macintosh, B., & Nadeau, D. 2006, ApJ, 641, 556
Matthews, B. C., Krivov, A. V., Wyatt, M. C., Bryden, G., & Eiroa, C. 2014, in Protostars and Planets VI, ed. H. Beuther et al. (Tucson, AZ: Univ. Arizona Press), 521
Matthews, E., Hinkley, S., Vigan, A., et al. 2017, ApJL, 843, L12
Mawet, D., Choquet, É., Absil, O., et al. 2017, AJ, 153, 44
Meshkat, T., Mawet, D., Bryan, M. L., et al. 2017, AJ, 154, 245
Metchev, S. A., & Hillenbrand, L. A. 2009, ApJS, 181, 62
Milli, J., Hibon, P., Christiaens, V., et al. 2017a, A&A, 597, L2
Milli, J., Vigan, A., Mouillet, D., et al. 2017b, A&A, 599, A108
Montesinos, B., Eiroa, C., Krivov, A. V., et al. 2016, A&A, 593, A51
Moór, A., Ábrahám, P., Derekas, A., et al. 2006, ApJ, 644, 525
Moór, A., Pascucci, I., Kóspál, Á., et al. 2011, ApJS, 193, 4
Morales, F. Y., Bryden, G., Werner, M. W., & Stapelfeldt, K. R. 2013, ApJ, 776, 111
Morales, F. Y., Bryden, G., Werner, M. W., & Stapelfeldt, K. R. 2016, ApJ, 831, 97
Mustill, A. J., & Wyatt, M. C. 2012, MNRAS, 419, 3074
Padgett, D., & Stapelfeldt, K. 2016, in IAU Symp. 314, Young Stars & Planets Near the Sun, ed. J. H. Kastner, B. Stelzer, & S. A. Metchev (Cambridge: Cambridge Univ. Press), 175
Pan, M., & Schlichting, H. E. 2012, ApJ, 747, 113
Patel, R. I., Metchev, S. A., Heinze, A., & Trollo, J. 2017, AJ, 153, 54
Pawellek, N., & Krivov, A. V. 2015, MNRAS, 454, 3207
Pawellek, N., Krivov, A. V., Marshall, J. P., et al. 2014, ApJ, 792, 65
Perrin, M. D., Duchene, G., Millar-Blanchaer, M., et al. 2015, ApJ, 799, 182
Preibisch, T., Ossenkopf, V., Yorke, H. W., & Henning, T. 1993, A&A, 279, 577
Pueyo, L. 2016, ApJ, 824, 117
Schneider, G., Grady, C. A., Hines, D. C., et al. 2014, AJ, 148, 59
Schneider, G., Grady, C. A., Stark, C. C., et al. 2016, AJ, 152, 64
Schneider, G., Silverstone, M. D., & Hines, D. C. 2005, ApJL, 629, L117
Schneider, G., Silverstone, M. D., Hines, D. C., et al. 2006, ApJ, 650, 414
Schneider, G., Smith, B. A., Becklin, E. E., et al. 1999, ApJL, 513, L127
Smith, B. A., & Terrile, R. J. 1984, Sci, 226, 1421
Soummer, R., Brendan Hagan, J., Pueyo, L., et al. 2011, ApJ, 741, 55
Soummer, R., Perrin, M. D., Pueyo, L., et al. 2014, ApJL, 786, L23
Soummer, R., Pueyo, L., & Larkin, J. 2012, ApJL, 755, L28
Stapelfeldt, K., Krist, J., Bryden, G., & Chen, C. 2007, in In the Spirit of Bernard Lyot: The Direct Detection of Planets and Circumstellar Disks in the 21st Century, ed. P. Kalas (Berkeley, CA: Univ. California), 47
Steele, A., Hughes, A. M., Carpenter, J., et al. 2016, ApJ, 816, 27
Strubbe, L. E., & Chiang, E. I. 2006, ApJ, 648, 652
Su, K. Y. L., Macgregor, M. A., Booth, M., et al. 2017, AJ, 154, 225
Thalmann, C., Janson, M., Buenzli, E., et al. 2013, ApJL, 763, L29
Thébault, P. 2009, A&A, 505, 1269
Thébault, P., & Wu, Y. 2008, A&A, 481, 713
Thureau, N. D., Greaves, J. S., Matthews, B. C., et al. 2014, MNRAS, 445, 2558
Vican, L., Schneider, A., Bryden, G., et al. 2016, ApJ, 833, 263
Wahhaj, Z., Milli, J., Kennedy, G., et al. 2016, A&A, 596, L4
Weinberger, A. J., Becklin, E. E., Schneider, G., et al. 1999, ApJL, 525, L53
Wisdom, J. 1980, AJ, 85, 1122
Woodward, C. E., Kelley, M. S. P., Harker, D. E., et al. 2015, ApJ, 809, 181
Wyatt, M. C. 2008, ARA&A, 46, 339